Plasma Enhanced Atomic Layer Deposition of Two-Dimensional WS_2 from WF_6, H_2 plasma and H_2S

Benjamin Groven[□,‡], Markus Heyne[□,‡], Ankit Nalin Mehta[‡,¬], Hugo Bender[‡], Thomas Nuytten[‡], Johan Meersschaut[‡], Thierry Conard[‡], Patrick Verdonck[‡], Sven Van Elshocht[‡], Wilfried Vandervorst[‡,¬], Stefan De Gendt[□,‡], Marc Heyns[‡,◊], Iuliana Radu[‡], Matty Caymax[‡], Annelies Delabie[□,‡]

□KU Leuven, Department of Chemistry, B-3001 Leuven, Belgium
‡IMEC, B-3001, Leuven, Belgium
¬KU Leuven, Department of Physics, B-3001 Leuven, Belgium
◊KU Leuven, Department of Materials Engineering, B-3001 Leuven, Belgium

Atomic Layer Deposition, transition metal dichalcogenides, WS_2, MoS_2, sub-surface reactions, 2D structure

ABSTRACT: Two-dimensional (2D) transition metal dichalcogenides are potential low dissipative semiconductor materials for nanoelectronic devices. Such applications require the deposition of these materials in their crystalline form and with controlled number of monolayers on large area substrates, preferably using growth temperatures compatible with temperature sensitive structures. This paper presents a low temperature Plasma Enhanced Atomic Layer Deposition (PEALD) process for 2D WS_2 based on a ternary reaction cycle consisting of consecutive WF_6, H_2 plasma and H_2S reactions. Strongly textured nanocrystalline WS_2 is grown at 300 °C. The composition and crystallinity of these layers depends on the PEALD process conditions, as understood by a model for the redox chemistry of this process. The H_2 plasma is essential for the deposition of WS_2 as it enables the reduction of $-W^{6+}F_x$ surface species. Nevertheless, the impact of sub-surface reduction reactions needs to be minimized to obtain WS_2 with well-controlled composition (S/W ratio of two).

INTRODUCTION − Two-dimensional (2D) materials are the subject of several recent advances in the field of catalysis[1–3], opto-electronics[4–6] and nanoelectronics[7,8]. In particular, the semiconducting 2D transition metal dichalcogenides (MX_2 with M a transition metal and X a chalcogen e.g. S, Se, Te), such as MoS_2 and WS_2 hold promise as semiconducting channel materials in ultra-scaled nanoelectronic devices, e.g. Metal-Oxide-Semiconductor Field Effect Transistors (MOSFETs) or Band-To-Band Tunnel Field-Effect Transistors (BTBT-FET)[7–11]. The main interest for these materials originates from the improved electrostatic gate control over the channel as compared to bulk Si, due to their monolayer thickness and planar structure. Furthermore, the MX_2 surface is in theory completely passivated as it is free of dangling bonds. The anticipated absence of defects at the semiconductor interface is interesting as they are a major source of mobility degradation in conventional semiconductors. Moreover, 2D materials are also interesting for monolithic 3D integration, in which stacks of circuits are sequentially fabricated on top of each other, a promising pathway to continuously increase device density[12]. In addition, the wide variety of MX_2 materials enables versatile combinations in van der Waals hetero-structures and opens new avenues for device physics and engineering[13–15].

The development of industrially relevant growth techniques for MX_2 is essential to further explore the potential of MX_2 materials and enable their integration for the proposed nanoelectronic applications. However, for use of MX_2 material as a semiconductor, a highly crystalline 2D structure, continuous MX_2 monolayers and defect-free interfaces are required. In addition, the growth technique should provide control of the number of monolayers over large area substrates as the MX_2 properties depend on the number of monolayers[16]. Currently Chemical Vapor Deposition (CVD) provides few layered MX_2 films with good semiconductor properties[17]. Continuous MX_2 films with micrometer-size crystal domains and monolayer thickness are obtained by CVD depending on the growth temperature (~400 °C–900 °C) from gas-phase metal-organic and halide precursors[18–23]. For MoS_2 and WS_2 CVD from the $Mo(CO)_6$ and $W(CO)_6$ precursors, the growth mode can be controlled over large substrates by controlling the reaction kinetics[19]. However, the reported processes require long deposition times. Kim et al. reported a self-limiting synthesis process based on the halide precursors, with the number of MX_2 layers depending on the growth temperature[21,22]. Alternatively, crystalline MX_2 materials can be obtained by chalcogenidation from metal or metal oxide[24,25]. However, this requires high temperatures (800 °C–1000 °C) and growth control down to a single monolayer remains challenging.

Atomic Layer Deposition (ALD) emerges as an interesting, alternative deposition technique to grow few-layered MX_2 with single layer growth control at low growth temperatures, compatible with temperature sensitive structures e.g. for the heterogeneous integration with existing Si nanotechnology. In ALD, thin films are grown by sequential self-limiting surface reactions of gas-phase precursors[26,27]. The self-limiting nature of the surface reactions ensures deposition with (sub-)monolayer control over large area substrates, as well as conformal deposition

on three-dimensional structures. By introducing a low temperature plasma in the reaction cycle, additional reactivity is provided to the surface, denoted as Plasma-Enhanced (PE-) ALD[28].

The feasibility of MoS_2 and WS_2 ALD is demonstrated in a limited number of reports[29–32]. Polycrystalline WS_2 films are deposited at a growth temperature of 300 °C–450 °C from tungsten hexafluoride (WF_6) and dihydrogen sulfide (H_2S) with addition of reducing agents such as diethylzinc, sacrificial Si layers and H_2 plasma[29,33]. Few reports demonstrated the growth of a polycrystalline MoS_2 film from another halide precursor $MoCl_5$ in combination with H_2S between 300 °C and 450 °C[30,34]. In addition, several groups report MoS_2 ALD processes from a metal-organic precursor, $Mo(CO)_6$, yielding amorphous layers at temperatures below 200 °C[31,35–37]. However, so far, the structural quality of most of the ALD grown films is limited, as the as-deposited layers are amorphous or polycrystalline with limited crystal grains sizes (in the order of several tens of nanometer). Nevertheless, Browning et al.[32] recently reported mobility values of ~12 cm^2/Vs for ALD grown WS_2 from WCl_5 and H_2S at 390 °C, which are in line with the values for CVD grown material, but lower than for exfoliated flakes of MX_2 material[17].

To optimize the structural quality of 2D MX_2 layers deposited by ALD, a better understanding of the growth mechanisms is required. A first requirement for creating highly crystalline structures is a low impurity content in the deposited layers. In addition, X deficiencies or vacancies, which can result in MO_x formation during air exposure, need to be avoided. Thus, understanding is needed on how the ALD process parameters affect the composition (M/X ratio) of the layers. This will imply an investigation of the redox mechanisms of the deposition process if the transition metal changes oxidation state during the ALD process.

Therefore, in this work, we present a detailed investigation in the growth mechanisms of the recently reported WS_2 PEALD process[33], where the PEALD reaction cycle consists of a WF_6, a H_2 plasma and a H_2S reaction. During the PEALD process, the W atom needs reduction from the +VI oxidation state in WF_6 to the +IV oxidation state in WS_2. We have investigated the impact of the deposition process parameters on the composition (S/W ratio) and 2D structure of the deposited films. Based on these results, we propose a model for the redox chemistry of the process. Finally, we discuss the influence of the growth temperature on the Growth-Per-Reaction-Cycle (GPC) of the PEALD process, and how it influences the 2D structure.

EXPERIMENTAL DETAILS − The WS_2 layers are deposited on 300 mm Si substrates covered with a 30 nm amorphous Al_2O_3 layer. The Al_2O_3 layer is deposited by ALD from trimethyl aluminum (TMA) and water (H_2O) at 300 °C. On the backside of the Si wafer, first a 50 nm Si_3N_4 film is deposited to prevent the WF_6 precursor from reacting with the silicon substrate during WS_2 deposition. The Si_3N_4 layer is deposited by PECVD at 400 °C from the silane (SiH_4) precursor, ammonia (NH_3), and nitrogen (N_2) plasma.

Next, WS_2 is deposited by PEALD from WF_6, H_2S (10 % H_2S in He, with 99.9 % pure H_2S) and H_2 plasma in a hot-wall, showerhead-type ASM PECVD reactor with direct (RF) plasma capability, connected to an Eagle12™ platform. Prior to deposition, the wafers are stabilized in the PECVD reactor for 5 minutes in N_2 (1000 sccm). The PEALD reaction cycle consists of three reactions: a WF_6 reaction, a H_2 plasma reaction and a H_2S reaction at a pressure of 2 Torr. Our best-known-method consists of 10 s of WF_6 (50 sccm), 10 s of H_2 plasma (500 sccm) at 100 W and 60 s of H_2S exposure (in He, 695 sccm) at 300 °C. These pulses are separated by a 20 s evacuation of the reactor to the base pressure of $1.5 \cdot 10^{-1}$ Torr. A He flow (450 sccm) minimizes diffusion of precursor gasses underneath the susceptor. The wafers are unloaded through a load-lock where they cool down in N_2 for 15 minutes before air exposure. In this work, the influence of the deposition temperature and plasma conditions among others are investigated. Therefore, the susceptor temperature is varied between 250 ºC and 450 ºC, whereas the temperature of the showerhead and the reactor walls remains constant at 225 °C and 175 °C respectively. The plasma power is varied between 100 W and 450 W.

A 30 nm amorphous Al_2O_3 layer is used as a substrate for the WS_2 PEALD at a deposition temperature of 300 °C. When growing WS_2 at deposition temperatures above 300 °C, a polycrystalline Al_2O_3 layer is used to avoid plasma-induced damage to the Al_2O_3 layer during the PEALD WS_2 process, as discussed in more detail in the *Supporting Information*. In that case, the amorphous Al_2O_3 layer is crystallized at a temperature of 900 °C in N_2 prior to the PEALD WS_2 process.

Optical Emission Spectroscopy (OES) measurements are performed to analyze the reactive species in the direct plasma (Figure 1a). A quartz optical fiber connected to an Ocean Optics USB2000+ spectrometer is attached to a viewport of the reactor, and collects the light emitted by the plasma. Primarily H atoms, H excited species and radicals, and molecular excited H_2 species are detected. The Balmer emission lines from electron impact excitation of atomic hydrogen in the ground state H_α and H_β are detected. In addition, the broad band between 550 nm–650 nm is the Fulcher band from molecular H_2[38–40]. This Fulcher band denotes the transition from the electronically excited state $d^3\prod_u$ to $a^3\sum_g^+$ by spontaneous radiative decay. Given the fairly high reactor pressure, the emission lines are broadened due to multiple short-range collisions between neutrals, and electrons and neutrals. This collisional line broadening impedes

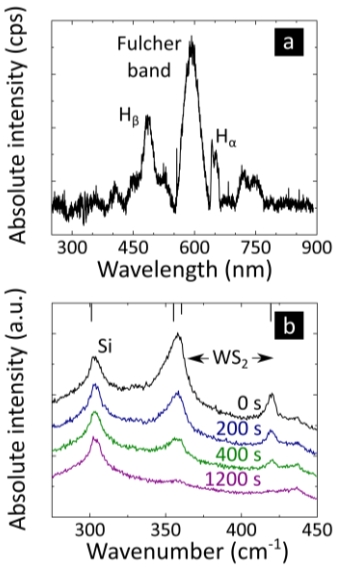

Figure 1. (a) Optical emission spectrum from a 100 W capacitively coupled H_2 plasma (13.56 MHz) recorded in the ASM PECVD reactor connected to an Eagle12-2 platform. (b) Raman spectra of 2 ML WS_2 as grown on 30 nm ALD Al_2O_3 at 300 °C as a function of the laser irradiation time from 0 s to 1200 s, using a vertical off-set between the individual spectra for clarity.

the detection of electron-impact excitation and ionization reactions.

The amount and composition, i.e. the S/W ratio, of the deposited layers are determined by Rutherford Backscattering Spectrometry (RBS) that quantifies the absolute amount of deposited W and S. The RBS measurements are carried out using a 1.52 MeV He+ ion beam and a scatter angle of 170 °. Furthermore, the WS_2 layer thickness is determined by Spectroscopic Ellipsometry (SE) for 21 points on the 300 mm wafer (edge exclusion of 3 mm) and performed on a KLA Tencor SCD100 system, assuming a single layer model for both the Al_2O_3 and the WS_2 layer. In addition, the composition and chemical bonds in the deposited WS_2 layers are determined by X-ray Photoelectron Spectroscopy (XPS). The measurements are performed in Angle Resolved (AR) mode using a Theta300 system from Thermo Instruments with a monochromatized Al Kα X-ray source (1486.6 eV) and a spot size of 400 µm. For all the spectra, the binding energies are referenced to the C1s peak. The peaks are fitted using pseudo-Voight functions (linear combination of Lorentzian and Gaussian) with fixed relative peak positions, after Shirley background subtraction.

The crystallinity of the deposited films is determined by X-Ray Diffraction (XRD, Cu Kα radiation, 50 kV, 30 mA) in a Bede MetrixL diffractometer from Jordan Valley. The XRD spectra are recorded for a 0.1° step size and 3 s step count, corrected for the background and fitted with a pseudo-Voight function. Additional information about the crystallinity and texture is obtained by cross-sectional High-Resolution Transmission Electron Microscopy (HR-TEM) using a FEI Tecnai F30 electron microscope operating at 300 kV. The WS_2 layer is transferred from the growth substrate to a Holey carbon TEM grid[41] for Plan-View TEM (PV-TEM) analysis of the crystal domain structure and size. For the PV-TEM analysis, a FEI TITAN electron microscope is used operating at 60 kV to minimize electron beam induced damage to the WS_2 in both Bright- (BF) and Dark-Field (DF). The WS_2 is transferred in a two-step process[24]: first a Poly(methyl methacrylate) (PMMA) film (3 % chlorobenzene) is spin coated on the WS_2 in two steps at 1000 rpm and 3000 rpm for 30 s respectively, and dry-baked (120 °C, 5 minutes). A thermal release tape is adhered to the PMMA. Afterwards, the sample is immersed in a H_2O bath (80 °C) for 15 minutes. Second, the WS_2 layers are separated from the substrate in a sonification bath, and after air-drying transferred to the TEM grid. Subsequently, the PMMA is dissolved in acetone (two hours) and the grid with transferred film is rinsed sequentially in isopropyl alcohol (IPA) and water (H_2O). The grid is stored in low vacuum until analysis.

The Raman Spectroscopy measurements are performed using a Horiba Jobin-Yvon HR800 Raman instrument at 532 nm laser excitation wavelength to evaluate the 2D structure of the WS_2. The excitating laser (~2.33 eV) resonates with the energy of the B exciton in bulk WS_2, that alters the relative intensities of the Raman modes compared to non-resonant Raman scattering and leads to both first and second-order Raman excitations[42,43]. The laser is operated at ~2 mW laser power with a laser spot size of 1 μm^2. A 300 µm confocal hole is used with a 1800 gr/mm grating. Single and few-layered WS_2 films degrade during laser irradiation. The absolute intensity of the Raman modes for WS_2 decreases as a function of the acquisition time during laser exposure time (Figure 1b). Most likely, the WS_2 layers degrade by a localized increase of the surface temperature during laser exposure[44]. We therefore fixed the acquisition time to 200 s to minimize the impact of laser induced degradation of the WS_2 layers, and avoid misinterpretation of the results. The Raman spectra are normalized to the Si peak at 300 cm^{-1} and corrected for the background by a blanket Si reference measurement. All peaks are de-convoluted into the individual Raman modes by using Voight functions.

RESULTS AND DISCUSSION – The paper is organized as follows. In section 1, we demonstrate that a strongly textured nanocrystalline WS_2 layer is grown by PEALD using a ternary reaction cycle of WF_6, H_2 plasma and H_2S at 300 °C. The WS_2 thickness is controlled by the number of PEALD reaction cycles. The crystallinity of WS_2 is characterized by both in- and

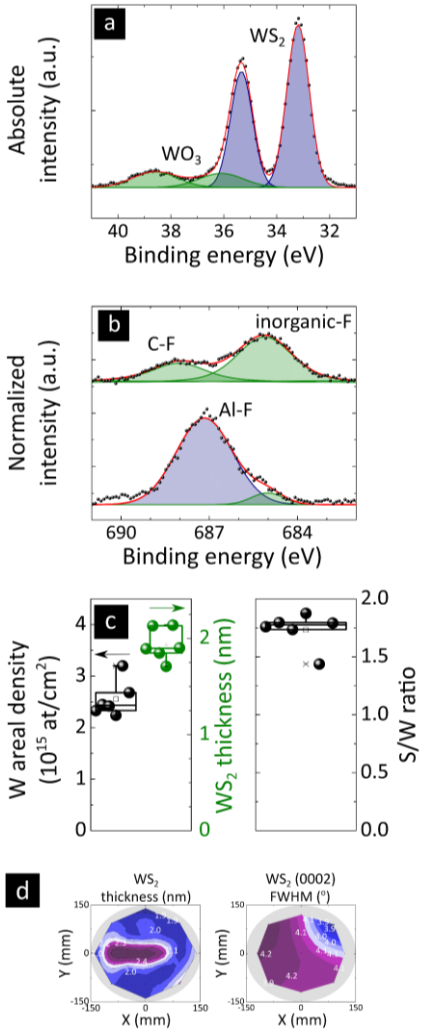

Figure 2. (a) W4f XPS spectrum of 3 ML WS_2 with corresponding peak deconvolution into WO_3 doublet (~36 eV) and WS_2 (~33 eV); (b) F1s XPS spectra of amorphous ALD Al_2O_3 layer (top), and PEALD WS_2 layer on ALD Al_2O_3 (bottom). The AlF_3 singlet (~687 eV) is observed suggesting the fluoridation of Al_2O_3 after PEALD WS_2; (c) W areal density (RBS), film thickness (SE) and the S/W ratio for a series of six wafers with 3 ML WS_2; and (d) wafer uniformity of the film thickness up to 11 % (SE, 21 measurement points) and the FWHM of the (0002) basal plane of 3 ML WS_2 (XRD, 9 measurement points). The ~3 ML WS_2 is grown on 30 nm amorphous ALD Al_2O_3 by the best-known method that consists of 10 s WF_6, 10 s and 100 W H_2 plasma and 60 s H_2S, and for a total of 65 PEALD reaction cycles at 300 °C.

out-of-plane TEM characterization. In section 2, we have analyzed the self-limiting behavior of the individual precursor reactions and the composition (S/W ratio) of the deposited layers by RBS and XPS. Based on these results, we propose a model that describes the redox mechanisms of the individual half-reactions of the reaction cycle (section 3). Finally, in section 4, we describe the impact of the growth temperature.

1. WS_2 DEPOSITION BY PEALD AT 300 °C – First, we characterize the WS_2 layers with a thickness of three monolayers (MLs), obtained by the PEALD at a growth temperature of 300 °C. The optimized reaction cycle, as will be further discussed below, consists of a WF_6 reaction of 10 s, a H_2 plasma exposure of 10 s at 100 W and a H_2S reaction of 60 s. The following overall reaction equation for deposition of WS_2 can be proposed:

$$WF_6 + x\ (H_2\ \text{plasma}) + 2\ H_2S \rightarrow WS_2 + 6\ HF + (x\text{-}1)\ H_2$$

In line with the formation of mainly WS_2, the amount of deposited S is about two times higher than the amount of W deposited, with the S/W of 1.8 ± 0.1 (RBS) and 1.9 ± 0.1 (XPS). XPS confirms the formation of mainly WS_2: the doublet in the W4f spectrum at a binding energy of ~33 eV and 35 eV indicates the presence of W–S bonds with W mainly in the +IV oxidation state (Figure 2a). No metallic W (~31 eV – 32 eV) is detected. In addition, minor contributions of WO_3 with W in the +VI oxidation state are identified by a second doublet at the binding energy of ~36 eV and 38 eV. The angular dependence of the XPS spectrum suggests that the WO_3 is present throughout the WS_2 layer, that is only ~2 nm thin. We presume that this small amount of WO_3 is formed during air exposure from S vacancies at and near the top surface and at grain boundaries (as will be discussed below) of the WS_2 layer.

F is detected at the interface between the WS_2 layer and the Al_2O_3 layer. During WS_2 PEALD, the surface of the Al_2O_3 layer is fluoridized and AlF_3 is formed, as determined from the XPS F1s spectrum at ~687 eV (Figure 2b). Either WF_6 or HF, a reaction by-product of the PEALD process, can directly fluoridize the Al_2O_3 substrate. The fluoridation of Al by repeated WF_6 exposures has been previously reported[45–47].

The uniformity of the layer thickness for a 3 ML WS_2 varies up to 11 % over the 300 mm substrate (Figure 2c), with the corresponding 300 mm wafer map of the layer thickness as determined by SE (Figure 2d). The wafer-to-wafer uniformity is 9 % for a series of six wafers (SE). RBS determines that the W areal density and the S/W ratio vary by 7 % and 3 % respectively between wafers, in agreement with SE. The outlier as indicated in the box plot is omitted from the calculation (Figure 2c).

X-Ray Diffraction (XRD, Figure 3a) indicates that the WS_2 layers have the 2D structure with interplanar distance ~0.65 nm as calculated from the (13.7 ±0.1) ° XRD peak position. It furthermore indicates that the films are nanocrystalline and highly textured, with the basal plane orientation parallel to the substrate surface. The corresponding 300 mm XRD wafer map of the FWHM of the (0002) basal plane confirms that WS_2 is deposited over the full wafer (Figure 2d). From a XRD rocking curve analysis, the tilt misorientation of the (0002) basal plane is only 0.15 °, indicating that the layers are highly textured and the WS_2 basal planes oriented parallel to the substrate (Figure 3b).

Cross-sectional HR-TEM confirms that the orientation of the WS_2 basal plane is parallel to the substrate (Figure 3c). The

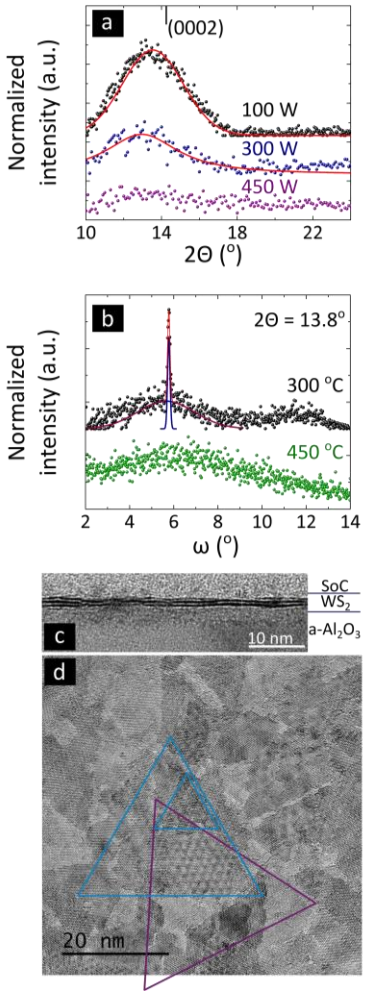

Figure 3. (a) XRD pattern of WS_2 for different plasma power (300 °C); (b) rocking curves for WS_2 (0002) reflection (2Θ = 13.8 °) at 300 °C and 450 °C; (c) High-resolution electron micrograph, and (d) corresponding plan view electron micrograph of WS_2 (300 °C). The highlighted triangles guide the eye and do not mark the grain boundaries, but rather indicate the symmetry of the inner regions. 3 ML WS_2 is grown on 30 nm amorphous ALD Al_2O_3 by the best-known method that consists of 10 s WF_6, 10 s and 100 W H_2 plasma and 60 s H_2S for a total of 65 PEALD reaction cycles. Only in the plan-view TEM, a thicker 5 ML WS_2 (130 PEALD reaction cycles) is used to highlight the growth of WS_2 on the WS_2 surface.

layer thickness varies locally between two and three single layers. HR-TEM indicates an (0002) inter-planar distance of 0.65 nm, in agreement with XRD. This value is slightly higher than reported in literature (0.62 nm) for natural bulk WS_2 crystals. The larger inter-planar distance could be induced by either strain in the polycrystalline layers, or due to intercalation of impurities.

In plain view along [0001], a mosaic structure of nanocrystalline 2D WS_2 domains is observed (Figure 3d). Different in-plane orientations of the WS_2 grains exist within a single layer and across the number of layers, as expected in the absence of a template for epitaxial seeding. The first WS_2 monolayer, which is formed on the amorphous Al_2O_3 surface, consists of several grains with different in-plane orientations. Indeed, an amorphous Al_2O_3 layer cannot provide an ordered template for

epitaxial seeding, explaining the different in-plane orientations of the grains. In contrast, some grains in the second WS_2 layer are in register with the underlying WS_2 monolayer, suggesting that epitaxial seeding on the WS_2 basal plane is possible (Figure 3d, in blue). Other grains in the second WS_2 layer have a different in-plane rotation than those in the first layer as indicated by Moiré patterns (Figure 3d, in purple). A grain in the second WS_2 layer might grow across a grain boundary of a grain in the first layer, explaining the difference in orientation.

The WS_2 domain sizes are broadly distributed up to 20 nm as determined from corresponding Dark-Field-TEM analysis (not shown). Given the nanocrystalline grain structure of the WS_2, we propose that next WS_2 layers grow either from a grain boundary or on the basal plane of the underlying WS_2 layer. The crystal edges of 2D materials generally have a higher reactivity than the basal planes[48–50].

Raman spectroscopy confirms that the WS_2 layer has the 2D structure. The following Raman modes are identified (Figure 4a): the second order longitudinal acoustic phonon mode 2LA(M) at 352 cm^{-1}, the in-plane optical mode $E^1_{2g}(\Gamma)$ at 356 cm^{-1} and the out-of-plane optical mode $A_{1g}(\Gamma)$ at 420 cm^{-1}. In addition, the first order in-plane optical mode at the M point $E^1_{2g}(M)$ can be observed at 330 cm^{-1}. The FWHM of these peaks and the signal intensity ratios (e.g. $2LA/A_{1g}$) are related to the WS_2 structural quality, while the relative differences in peak positions can be correlated to the number of WS_2 monolayers[42,51]. The 2LA(M) mode appears as the prominent mode for the PE-ALD grown WS_2 at the laser excitation wavelength of 532 nm, irrespective of the number of layers, in agreement with literature[52]. The FWHM of this 2LA(M) mode can be used as a qualitative measure for local disorder in the atomic ordering of the in-plane WS_2 crystal lattice[52]. The as grown 3 ML WS_2 has a slightly larger FWHM as compared to exfoliated bulk crystals

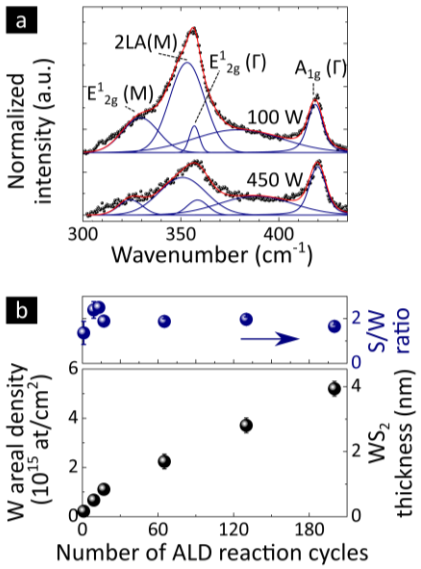

Figure 4. (a) Raman spectra for 3 ML WS_2 with peak deconvolution and assignment (inset) for 100 W and 450 W H_2 plasma power (65 PEALD reaction cycles); (b) The W areal density, WS_2 thickness and S/W ratio as a function of the number of PEALD reaction cycles as determined by RBS on a 30 nm amorphous ALD Al_2O_3 layer. The steady-state GPC is ~0.017 nm/cycle. The WS_2 is grown with the best-know method at 300 °C. WS_2 thickness is extracted from the W areal density (RBS) and the atom density.

Table 1. FWHM of the prominent Raman modes for 3 ML WS_2 as grown by PEALD by the best-known method (65 PEALD reaction cycles, 300 °C), and pristine and exfoliated (bulk) WS_2, on 30 nm ALD Al_2O_3 layer.

FWHM (cm^{-1})	PEALD WS_2	Pristine WS_2
2LA(M)	20.5 ± 0.8	8.9 ± 0.5
$E^1_{2g}(\Gamma)$	5 ± 2	3.6 ± 0.3
$A_{1g}(\Gamma)$	9 ± 2	3.5 ± 0.5

(Table 1), which suggests that the PEALD WS_2 shows some disorder in the crystal lattice.

Second, the growth curve of the PEALD process indicates that the thickness of the WS_2 layer is well-controlled by the number of PEALD reaction cycles. In the bulk regime, the WS_2 thickness increases linearly with the number of PEALD reaction cycles and the steady Growth-Per-Cycle (GPC) for deposition at 300 °C is $(2.2\pm0.1)\cdot10^{13}$ W atoms/cm^2/cycle (RBS) or ~0.017 nm/cycle (Figure 4b). As in a perfectly crystalline WS_2 monolayer, the areal density is $1.16\cdot10^{15}$ W atoms/cm^2, the amount of deposition per PEALD reaction cycle is only ~2 % of the monolayer. The low GPC value is most likely related to the low reactivity of the WS_2 crystal basal planes, and will be explained more in detail from the proposed growth model in section 3.3. As demonstrated above, the WS_2 layer is nanocrystalline but highly textured, and the top surface is proposed to consist mainly of the S-terminated WS_2 basal planes of the crystals. It has been demonstrated that the basal planes of 2D MX_2 materials have a rather low reactivity towards ALD[48–50], which could explain the low value of the GPC in the PEALD process.

In line with this, a higher growth-per-cycle of $(5.6\pm0.1)\cdot10^{13}$ W atoms/cm^2/cycle (or ~0.042 nm/cycle) is observed in the first 30 PEALD reaction cycles on the Al_2O_3 substrate, indicating substrate enhanced growth. That is, the Al_2O_3 surface is more reactive towards the PEALD precursors compared to the WS_2 layers. The WF_6 precursor chemisorbs on the Al_2O_3 surface from the first PEALD reaction cycle, and the Al_2O_3 surface becomes fluoridized as well. The GPC decreases with the number of PEALD reaction cycles and eventually stagnates to the steady value of $(2.2\pm0.1)\cdot10^{13}$ W atoms/cm^2/cycle (or ~0.017 nm/cycle). Thus, as the Al_2O_3 substrate gets covered by the deposited WS_2 layer, the surface becomes less reactive towards PEALD.

2. INVESTIGATION OF THE PEALD HALF-REACTIONS (300 °C) – Next, we investigate the individual half-reactions in the PEALD process, and how the precursor doses affect the amount of deposition, the composition (S/W ratio) and 2D structure of the as-deposited layers. The growth temperature is fixed at 300 °C. To minimize the potential impact of the starting surface and study the WS_2 deposition in the steady growth regime, the reaction cycle is repeated 65 times.

The *WF_6 reaction*, the first reaction in the ternary PEALD reaction cycle, shows the ALD saturation behavior, indicative of a self-limiting surface reaction. The amount of deposited W saturates readily with WF_6 exposure time to a value of $(3.0\pm0.1)\cdot10^{13}$ W at/cm^2/cycle or ~0.022 nm/cycle (RBS, Figure 5a). In line with the formation of WS_2, the amount of deposited S is about two times higher than the deposited W content, with the S/W varying between 1.7±0.1 and 1.9±0.1, irrespective of the WF_6 exposure time. In the next experiments, we will fix the WF_6 exposure time to 10s in the saturation region.

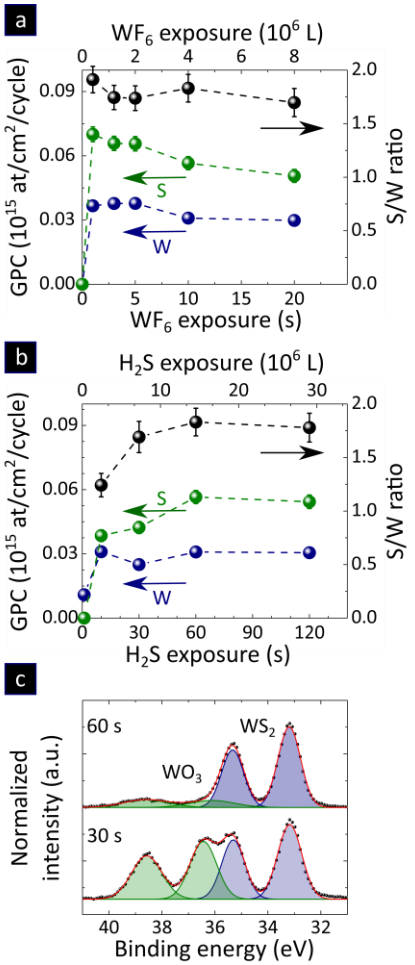

Figure 5. (a) W and S GPC and S/W ratio (RBS) as a function of WF_6 exposure per reaction cycle (in seconds and Langmuir) for constant 10 s, 100 W H_2 plasma and 60 s H_2S; (b) W and S GPC and S/W ratio (RBS) as a function of the H_2S exposure (in seconds and Langmuir) for constant 10 s WF_6 and 10 s, 100 W H_2 plasma; and (c) W4f XPS spectra of 3 ML WS_2 as grown for different H_2S pulses. The WS_2 is grown on 30 nm amorphous ALD Al_2O_3 (300 °C) for a fixed number of PEALD reaction cycles (65). The dotted lines are guide to the eye.

The *H_2S reaction*, the last reaction in the ternary PEALD reaction cycle, also shows the conventional ALD saturation behavior for both the W and S content, similar to the WF_6 reaction (Figure 5b). Saturation of the amount of deposited W and S is observed for H_2S exposures times of 60 s (corresponding to H_2S exposures of $1.4{\cdot}10^7$ L) and longer. The S/W ratio is 1.8±0.1 in this saturation region, confirming the formation of mainly WS_2. For too short H_2S exposures, between 10 s and 60 s, S deficient layers are obtained with a S/W ratio that is systematically lower than two. XPS indicates that after air exposure, the layers consist of both WS_2 and WO_3 (Figure 5c). For 1s H_2S exposures, much less W and almost no S is deposited, with the S content below the detection limit of RBS ($< 2{\cdot}10^{14}$ at/cm^2). The surface reaction of H_2S is less efficient than the surface reaction of WF_6. The reaction efficiency is estimated by dividing the amount of deposited W or S on the 300 mm wafer surface by the total amount of W or S introduced in the reactor by WF_6 or H_2S. For WF_6, the reaction efficiency is $1.2{\cdot}10^{-3}$ %, while for the H_2S the reaction efficiency is only $2.2{\cdot}10^{-6}$ %. As a result, a long exposure time of 60 s H_2S (or $1.4{\cdot}10^7$ L) is required to deposit WS_2 at 300 °C.

The *H_2 plasma reaction* is essential for the WS_2 deposition at 300 °C: when the plasma pulse is left out of the reaction cycle, using only sequential WF_6 and H_2S exposures, no WS_2 is deposited on the Al_2O_3 surface. The deposited amounts of W and S are below the limits of quantification of RBS ($1{\cdot}10^{13}$ W atoms/cm^2 and $2{\cdot}10^{14}$ S atoms/cm^2) irrespective of the deposition conditions tested (up to 10 s WF_6 and 60 s H_2S), and only deposition of F is observed on the surface (~$3{\cdot}10^{15}$ F at/cm^2 , XPS).

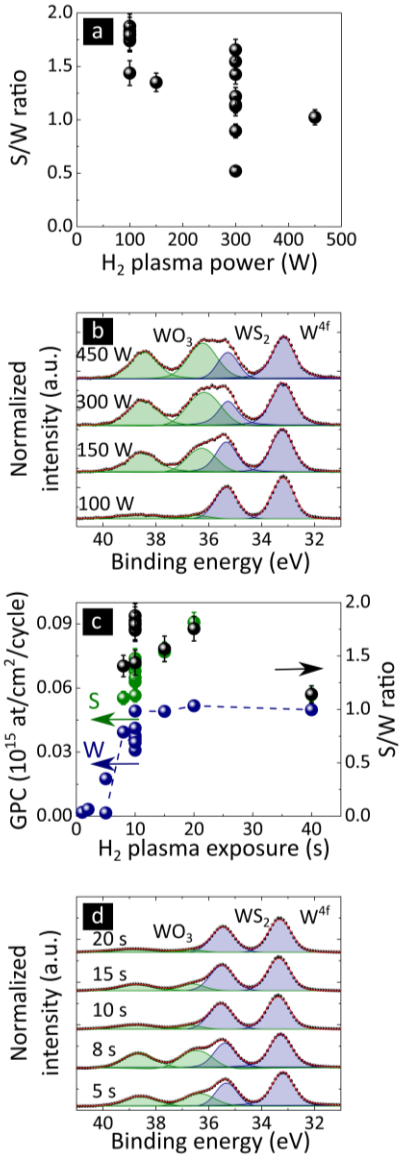

Figure 6. (a) S/W ratio as a function of H_2 plasma power, for constant 10 s WF_6, 10 s H_2 plasma and 60 s H_2S reaction. (b) Corresponding W4f XPS spectra for increasing H_2 plasma power; (c) W and S GPC and S/W ratio as a function of H_2 plasma exposure per reaction cycle (in seconds) for constant 10 s WF_6 and 60 s H_2S reaction, and for 100 W H_2 plasma power; (d) Corresponding W4f XPS spectra for increasing H_2 plasma exposure time. The WO_3 doublet (~36 eV) and WS_2 (~33 eV) are indicated. The WS_2 is grown at 300 °C on 30 nm amorphous ALD Al_2O_3 for a fixed number of PEALD reaction cycles (65). The dotted lines are guide to the eye.

Table 2. Growth model for the proposed ternary PEALD reaction cycle consisting of a WF_6, H_2 plasma and H_2S reaction.

WF_6	Surface	$-W-SH_{(s)} + WF_{6(g)}$	→	$-W-S-WF_{(6-x)(s)} + x\ HF_{(g)}$
		$WS_{2(s)} + WF_{6(g)}$	→	$WS_2-WF_{6(s)}$
H_2 plasma	Surface	$-S-WF_{6-x(s)} + ½(6-x)\ H_{2(plasma)}$	→	(1) $-S-W^0_{(s)} + (6-x)\ HF_{(g)}$
		$-S-WF_{6-x(s)} + ½(7-x)\ H_{2(plasma)}$	→	(2) $-S-WH_{(s)} + (6-x)\ HF_{(g)}$
		$-S-WF_{6-x(s)} + ³⁄₂x\ H_{2(plasma)}$	→	(3) $-S-WF_{6-2x}H_{2x(s)} + x\ HF_{(g)}$
	Bulk	$WS_{2(s)} + 2\ H_{2(plasma)}$	→	(1') $W^0_{(s)} + 2\ H_2S_{(g)}$
		$2\ WS_{2(s)} + 3\ H_{2(plasma)}$	→	(2') $2\ S-W-H_{(s)} + 2\ H_2S_{(g)}$
H_2S	Surface	(1) $2\ -W^0_{(s)} + 2\ H_2S_{(g)}$	→	$2\ -W-SH_{(s)} + H_{2(g)}$
		(2) $-WH_{(s)} + H_2S_{(g)}$	→	$-W-SH_{(s)} + H_{2(g)}$
		(3) $-WF_{6-2x}H_{2x(s)} + H_2S_{(g)}$	→	$-W-SH_{(s)} + (6-2x)\ HF_{(g)} + (2x-⁵⁄₂)\ H_{2(g)}$
	Bulk	(1') $W^0_{(s)} + 2\ H_2S_{(g)}$	→	$WS_{2(s)} + 2\ H_{2(g)}$
		(2') $2\ S-W-H_{(s)} + 2\ H_2S_{(g)}$	→	$2\ WS_{2(s)} + 3\ H_{2(g)}$

The model assumes that the surface is saturated with –SH sites during the steady-state deposition and that gas-phase reactions are neglected. Only the growth of WS_2 on the closed and continuous WS_2 surface is considered neglecting the impact of the starting substrate. The individual H_2 plasma and H_2S reactions are separated into a surface and sub-surface ('bulk') reaction pathway with the WS_2 film. (s): solid phase, (g): gas phase.

In contrast, WS_2 deposition is enabled by including a H_2 plasma reaction in between the WF_6 and H_2S reactions, at least in a confined window for the H_2 plasma parameters. While both the WF_6 and H_2S reactions show ALD-like saturation behavior, a more complex reactivity is observed for the H_2 plasma reaction. Both H_2 plasma power and exposure time affect the composition of the WS_x layer. The deposition of WS_2 is observed for a low H_2 plasma power of 100 W, and the S/W ratio of nearly two is repeatable from wafer to wafer (Figure 2c). When the H_2 plasma power increases, the S content in the layers decreases (RBS, Figure 6a) and the amount of WO_3 significantly increases (XPS, Figure 6b). This is understood from the reduction of the WS_2 layers by the H_2 plasma to W that during the ex-situ XPS analysis oxidizes to WO_3. In addition, the repeatability of the composition from wafer to wafer severely degrades at higher plasma power. The poor wafer-to-wafer repeatability is clearly illustrated for a plasma power of 300 W, where the S/W ratio ranges between 0.6 and 1.6 (Figure 6a). In addition to S deficiencies in the WS_x layer, the too strong H_2 plasma power and/or time even induce damage to the underlying Al_2O_3 layers, as blisters form at the interface between the Al_2O_3 film and the Si substrate.

The H_2 plasma exposure also affects the composition of the deposited layers. Too short plasma exposures, e.g. 1 s and 2 s, result in a negligible amount of W and S deposition, indicating no activity of the H_2 plasma, similar as for the thermal WF_6 and H_2S reaction cycle. For a fixed H_2 plasma power of 100 W, H_2 plasma exposure times between 10 s and 20 s result in well-repeatable depositions of WS_2 (Figure 6c,d). Furthermore, the blister formation is not observed. Thus the combination of low, 100 W H_2 plasma power and 10 s exposure yields repeatable WS_2 deposition and no damage to the underlying Al_2O_3 layers (Figure 6d). In line with that, this condition results in the best structural quality of the WS_2 monolayers, as the Raman features are most pronounced. When the H_2 plasma power increases, the FWHM of the 2LA(M) mode increases, indicating that the 2D structure deteriorates as the S content in the WS_x layers decreases (Figure 4a). The degradation of the 2D structure is further confirmed by XRD, the (0002) diffraction peak gradually decreases with increasing H_2 plasma power (Figure 3a). For 450 W, no characteristic features are observed in XRD. The 2D structure is obviously affected by the composition of the 2D material.

To conclude, the composition of the layer (the S/W ratio) is strongly determined by the H_2 plasma and H_2S reaction conditions. The H_2 plasma is essential for WS_2 deposition, but nevertheless the reactivity of the H_2 plasma should be limited to avoid the formation of S-deficient layers and blisters underneath the underlying Al_2O_3 layers. On the other hand, the H_2S reaction is slow and extensive H_2S exposures are needed to avoid the formation of S-deficient layers.

3. MODEL FOR THE REDOX CHEMISTRY OF THE WS_2 PEALD – We now propose a model for the chemisorption reactions and redox reaction mechanisms of the bulk WS_2 PEALD process, based on the experimental observations as described above (Table 2).

During the *WF_6 exposure*, WF_6 chemisorbs on the WS_2 surface and the surface reaction is self-limiting, as indicated by the observed saturation behavior (Figure 5a). The reactive surface sites for WF_6 reaction can be either surface S atoms or –SH groups, created by the H_2S reaction in the preceding reaction cycle, and volatile HF is released as reaction product. As no reducing agent is present and as the deposition temperature is low, we can presume that the W atoms remains in the +VI oxidation state after chemisorption.

The –SH groups are created during the precedent H_2S reaction and most likely exist only at the edges of the WS_2 crystals and not on the WS_2 basal planes. According to literature, the adsorption of H atoms on the S passivated basal planes is energetically unfavorable[53–55]. The S passivated basal plane of WS_2 is anticipated to be less reactive than the crystal edges. However, from our current investigation we cannot exclude that reactions at the WS_2 basal plane occur. TEM reveals that some of the WS_2 layers are grown in registry with underlying WS_2 grains. Therefore direct van der Waals epitaxy on the WS_2 basal plane cannot be excluded, initiated by weak adsorption of WF_6 on the basal planes or through S vacancies or interstitials.

In the subsequent *H_2 plasma reaction*, these $-WF_x$ surface species are reduced from the +VI oxidation state to lower oxi-

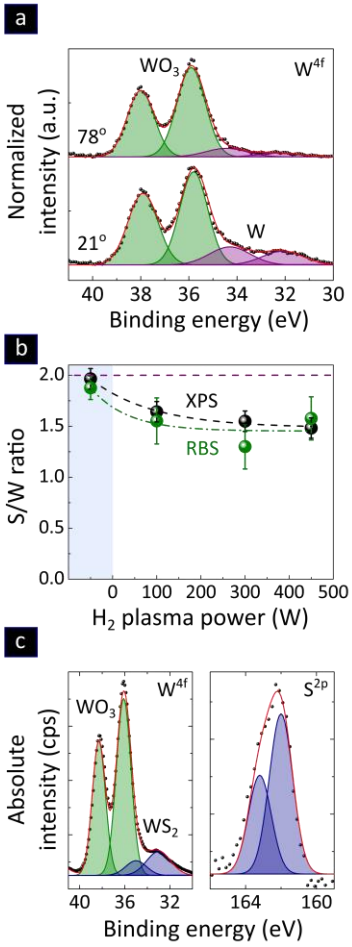

Figure 7. (a) Angle-Resolved W4f XPS spectra for a 0.5 nm W film grown by a PEALD process of WF_6 and H_2 plasma at 300 °C, and measured at exit angles of 21 ° and 78 ° with respect to the normal of the substrate (65 PEALD reaction cycles of 10 s WF_6 and 10 s H_2 plasma, 100 W, 300 °C); (b) S/W ratio as a function of the H_2 plasma power as determined by XPS and RBS for an as grown 3 ML WS_2 layer exposed to a H_2 plasma (600 s). The dotted lines are guide to the eye; and (c) the Angle-Integrated W4f and S2p XPS spectra for a 0.5 nm W film grown by a PEALD process of WF_6 and H_2 plasma at 300 °C after a single H_2S reaction of 60 s or $1.4 \cdot 10^7$ L at 300 °C.

dation states, with the formation of HF as highly volatile reaction product. We have confirmed that reduction is indeed possible, as even metallic W can be deposited by WF_6/H_2 plasma PEALD process in the same conditions of the H_2 plasma. The presence of metallic W was confirmed by XPS (Figure 7a), and similar amounts of F were detected when compared to WS_2 deposition (up to $3.0 \cdot 10^{13}$ W at/cm^2). Note that the layer was partly oxidized to WO_3 during air exposure as the XPS analysis was performed ex-situ. The WF_6/H_2 plasma PEALD of W at temperatures between 300 °C and 400 °C has also been reported previously in the literature[56].

However, in the case of too strong H_2 plasma conditions in the WS_2 PEALD process, the reduction reaction is not confined to the top surface only, and contributions from sub-surface reactions also play a role. The reduction reaction of the WS_2 layers by the H_2 plasma was verified by exposing 3 ML of WS_2 to a H_2 plasma for different plasma powers. Indeed, the S/W ratio decreases from ~1.9 in the as grown WS_2 to 1.5 after plasma exposure, as determined by XPS and RBS (Figure 7b). This confirms that the H_2 plasma reduces part of the WS_2 layer creating a S-deficient layer prone to oxidation in air. Aggressive plasma conditions (plasma power higher than 100 W, plasma exposure times longer than 20 s) not only result in the formation of S-deficient layers, but also create damage to the underlying Al_2O_3 layers. Thus, the plasma parameters need to be carefully controlled to confine the reduction as much as possible to the top surface only.

The formation of WS_2 occurs by sulfidation by the *H_2S reaction*, the final reaction in the PEALD reaction cycle. This oxidation reaction yields W in the final +IV oxidation state. H_2S can sulfidize the metallic W or W in intermediate oxidation states at and near the top surface at the relatively low PEALD temperature of 300 °C. Indeed, we demonstrate this by the in-situ reaction of H_2S with thin W layers. First, a metallic W layer of $(1.4 \pm 0.1) \cdot 10^{15}$ W at/cm^2 is deposited by 65 reaction cycles of the WF_6/H_2 plasma PEALD. Next, this W layer is exposed to a single H_2S reaction of 60 s or $1.4 \cdot 10^7$ L at 300 °C, as used in the PEALD WS_2 reaction cycle. WS_2 formation is evidenced by XPS from both the W4f 7/2 doublet (at ~33 eV) and the S2p doublet (Figure 7c). This experiment also indicates that the diffusion of H_2S in the W layer is limited at the low temperature of 300 °C: W layers of $(1.4 \pm 0.1) \cdot 10^{15}$ W at/cm^2 are only partly sulfidized, with about $0.3 \cdot 10^{15}$ W at/cm^2 converted into WS_2 (RBS). The amount of S deposited per PEALD WS_2 reaction cycle is $(4.0 \pm 0.2) \cdot 10^{13}$ S at/cm^2/cycle. Therefore we conclude that H_2S can oxidize W surface species even at growth temperatures as low as 300°C, provided that the amount of reduced W species formed during the H_2 plasma reaction is limited.

Thus, for the H_2S to sulfidize all the W formed during the H_2 plasma exposure, the H_2 plasma reaction needs to be confined to the surface of the WS_2. That is, the hydrogen plasma cannot reduce more W at and below the surface by sub-surface reactions than can be sulfidized during the next H_2S reaction. Thus, the H_2 plasma conditions need to be carefully controlled to minimize these sub-surface reactions and as such the composition of the WS_2 is controlled. This can be achieved by using mild H_2 plasma conditions (100 W, 8 s–20 s) in combination with long H_2S exposures of 60 s. When too aggressive H_2 plasma conditions are applied (300 W–450 W, > 20 s), or too short H_2S exposures (< 60 s), the layers are S deficient layers as both WS_2 and metallic W is present, the latter being oxidized to WO_3 by air exposure (Figure 2a).

To conclude, the H_2 plasma and H_2S reactions have an opposite reactivity in terms of redox behavior, with reduction occurring during the H_2 plasma reaction and oxidation occurring during the H_2S reaction. Mild H_2 plasma conditions are needed (100 W and exposure times between 10 s and 20 s) to enable WS_2 deposition. In that case, the reduction and oxidation reactions at (and possibly near) the top surface are completely balanced. Whether or not contributions from subsurface reactions occur in these conditions cannot be concluded from the current investigation and would require further investigations by in-situ characterization techniques. In contrast, sub-surface reactions clearly play a role in the case of aggressive H_2 plasma conditions (higher plasma power or longer plasma exposure time), and explain the formation of S deficient WS_x layers. Note that sub-surface reactions have been previously proposed to contribute in other ALD processes, such as Pt-group metals including Ru and Pt ALD[57–60].

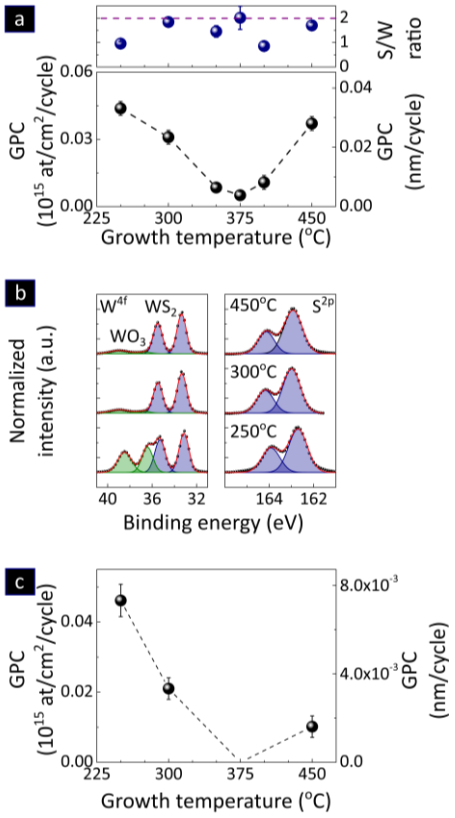

Figure 8. (a) W and S GPC and the S/W ratio as determined by RBS, and the corresponding WS_2 GPC (in nm/cycle) of the PEALD WS_2 as a function of the deposition temperature. (b) W4f and S2p XPS spectra of the WS_2 PEALD process for three different deposition temperatures. The spectra are aligned to the maximum intensity to simplify chemical comparison, and shifted vertically at fixed off-set for clarity. The WS_2 is grown by the best-known method for a 10 s WF_6, 10 s and 100 W H_2 plasma and 60 s H_2S reaction (65 PEALD reaction cycles). (c) The W GPC as determined by RBS and the corresponding W GPC (in nm/cycle) as a function of the deposition temperature for the PEALD W process. The W layers are grown by a PEALD reaction cycle consisting of a 10 s WF_6, 10 s and 100 W H_2 plasma (65 PEALD reaction cycles). A polycrystalline 30 nm ALD Al_2O_3 is used for all deposition temperatures. The dotted lines are guide to the eye.

Finally, the proposed reaction mechanism can also explain the low value of the GPC in the PEALD process of $(2.2\pm0.1)\cdot10^{13}$ W atoms/cm^2/cycle (RBS) (~0.017 nm/cycle or 2 % of a WS_2 monolayer). The density of –SH sites on the surface is anticipated to be low, as –SH groups exist only at the edges of the WS_2 crystals and not on the basal plane[53]. In addition, direct van der Waals epitaxy on the WS_2 basal plane can occur by weak adsorption of WF_6 on the basal planes or through S vacancies or interstitials.

4. PEALD TEMPERATURE WINDOW – Next, we investigate the impact of the deposition temperature of the WS_2 PEALD process on the GPC and the structure of the WS_2 layer. We have fixed the PEALD reaction cycle at the optimal conditions for 300 °C, and we also fixed the number of reaction cycles (65) to determine the GPC. As the GPC for each deposition temperature is calculated as the average after a fixed number of reaction cycles, there might be an influence of the substrate on the nucleation of the first WS_2 layers and that nucleation behavior can also depend on the deposition temperature.

We observe that the composition of the deposited layers strongly varies with the deposition temperature between 250 °C and 450 °C. WS_2 with a S/W ratio of 1.8 ± 0.1 (RBS, XPS) is grown only at deposition temperature of 300 °C and 450 °C (Figure 8a,b). The formation of WS_2 suggests that the reduction and oxidation reactions are balanced, although the contribution of sub-surface reactions cannot be excluded. In contrast, at 250 °C, the S/W ratio is significantly lower than two (~1, RBS) and the layers are partially oxidized after air exposure. This indicates that the sulfidation reaction occurs slower at lower deposition temperature, while the reduction reaction by H_2 plasma is less affected. The H_2S reaction does not reach saturation at 225 °C. Therefore, not all deposited W species are sulfidized, resulting in S deficient layers that consist of WS_2 and WO_3 after air exposure. Thus, it will be necessary to adjust the H_2 plasma and H_2S conditions to yield deposition of WS_2 at this lower deposition temperature. Fluoridation of the Al_2O_3 substrate occurs irrespective of the deposition temperature: between $2\cdot10^{15}$ and $3\cdot10^{15}$ F at/cm^2 are detected by XPS, with F bonded mainly to Al.

We do not observe a temperature window where the GPC remains constant, even though the PEALD half-reactions of WF_6 and H_2S are self-limiting at 300 °C. Instead, the amount of deposited W first decreases and then again increases with the deposition temperature. The average GPC in the first 65 reaction cycles first decreases from $(4.5 \pm 0.1)\cdot10^{13}$ at/cm^2/cycle at 250 °C to $(0.5 \pm 0.1)\cdot10^{13}$ at/cm^2/cycle at 400 °C (Figure 8a). Only small amounts of W are deposited between 350°C and 400 °C. At 450 °C, the GPC again increases to $(3.0 \pm 0.1)\cdot10^{13}$ at/cm^2/cycle. A similar temperature dependence is observed for the W PEALD process from the WF_6 precursor and H_2 plasma (Figure 8c). That is, the average W GPC decreases with the growth temperature between 250 °C and 375 °C, and increases again for temperatures up to 450 °C. At all growth temperatures, up $3\cdot10^{15}$ F at/cm^2 are detected, similar as observed for the PEALD WS_2 process.

The temperature dependence of the GPC might relate to how the deposition temperature influences the individual surface reactions, in line with the proposed model for the redox chemistry of the WS_2 PEALD process. Furthermore, since the influence of the starting substrate cannot be excluded here, the nucleation of WS_2 on the starting surface can depend on the deposition temperature and as such influence the GPC. Even though the amount of AlF_3 was found to be independent of the deposition temperature, the nucleation of WS_2 might still be temperature dependent. Note that the starting substrate, the deposition temperature and the type of reactant used in the reaction cycle for W ALD processes from WF_6 and Si_2H_6 (or SiH_4) have shown to influence the nucleation behavior of W films[61–64]. It is unlikely the increase in GPC at 450 °C is related to thermal decomposition of the WF_6 precursor, as WF_6 starts to decompose only at temperatures above 750 °C[65].

In conclusion, further investigation of the saturation behavior of the PEALD process at different deposition temperatures as well as the corresponding nucleation behavior is beyond the scope of this investigation as our results show that this might be very complex. Our proposed reaction mechanism nevertheless gives the necessary insight that can guide the further development of WS_2 growth at different temperatures.

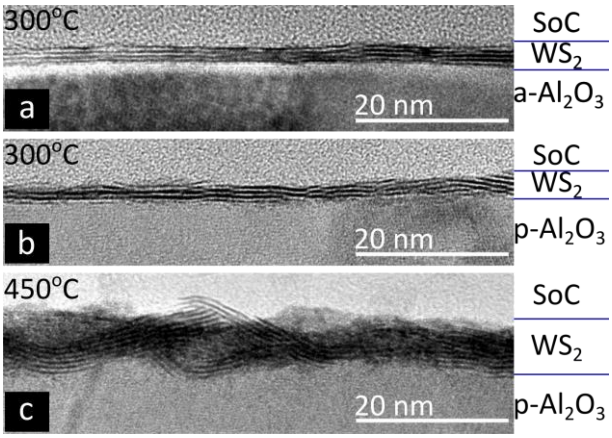

Figure 9. High-resolution transmission electron micrograph of 3 ML WS_2 as grown on (a) amorphous and (b) polycrystalline 30 nm ALD Al_2O_3 for 65 PEALD reaction cycles at 300 °C; and (c) High-resolution electron micrograph of 6 ML WS_2 on polycrystalline 30 nm ALD Al_2O_3 for 130 PEALD reaction cycles at 450 °C. The WS_2 is grown by the best-known method that consists of a 10 s WF_6, 10 s and 100 W H_2 plasma and 60 s H_2S reaction. For TEM specimen preparation, the layers are coated with a Spin-On-Carbon layer.

Finally, the deposition temperature also affects the crystallinity of the WS_2, in particular the orientation of the crystal basal planes with respect to the substrate, as reported previously[29,33]**Error! Bookmark not defined.**,**Error! Bookmark not defined.**. At 300 °C, the WS_2 has the preferential (0002) orientation (Figure 9a-b), and a low mean spread in orientation of the basal plane with a (0002) tilt misorientation of ~0.15 ° (Figure 3a-b). In contrast, the orientation between the different crystal grain basal planes becomes more random at the higher growth temperature of 450 °C. That is, the basal planes are locally misaligned and oriented out-of-plane as evidenced by HRTEM micrographs (Figure 9c). Note that WS_2 is expected to be mechanically strong and flexible, comparable to MoS_2 (with elastic bending modulus of 9.61 eV for monolayer MoS_2[66]), which might explain the bending of the (0002) planes that can be observed locally. At 450 °C, the WS_2 has a weakly (0002) textured component, as suggested by the broadening of the rocking curve (Figure 3b). No sharp feature is observed, suggesting large and random (0002) orientation. The WS_2 layer was grown on polycrystalline Al_2O_3 at 450 °C in order to avoid the formation of blisters (cf. Supplementary Information). The higher surface roughness of the polycrystalline Al_2O_3 layer (~0.3 nm, AFM) might contribute to the more random orientation of the WS_2 (0002) basal planes.

CONCLUSIONS – The composition, purity and the crystallinity of semiconductors directly influences the semiconductor properties and therefore these need to be carefully controlled in ALD processes for 2D MX_2 materials. This paper presents an insight in the growth mechanisms of a ternary PEALD process for WS_2 layers at 300 °C, using a reaction cycle with WF_6, H_2 plasma and H_2S pulses. Nanocrystalline, strongly textured WS_2 layers with controlled composition (S/W ratio) are grown on amorphous Al_2O_3 substrates. This is realized by confining the reactions to the surface and by minimizing contributions from sub-surface reduction reactions during the H_2 plasma reaction. This is provided that the amount of W surface species formed during the H_2 plasma reaction can be sulfidized during the H_2S reaction, which is slow at the low deposition temperature of 300 °C. Such sub-surface reactions have also been reported in other ALD processes and typically lead to impurities and defects in the films. In particular for 2D materials, with a high surface to volume ratio, such sub-surface reactions should be avoided.

Finally, also the nucleation mechanisms in ALD processes determine the crystallinity of the deposited layers. As such, further research is needed to obtain fundamental understanding of the nucleation mechanisms of ALD grown MX_2 material, and the impact on the 2D structure (e.g. domain size and alignment) and semiconductor properties.

ASSOCIATED CONTENT

Supporting Information. H_2 plasma reaction with the ALD Al_2O_3 layer as a function of plasma conditions and susceptor temperature, as supported by optical microscopy and depth-profile analysis of the Al_2O_3 layers. This material is available free of charge via the Internet at http://pubs.acs.org.

AUTHOR INFORMATION

Corresponding Author

* Annelies.Delabie@imec.be

Author Contributions

All authors have given approval to the final version of the manuscript.

Funding Sources

B. G. and M. H. acknowledge the funding from the Agency for Innovation by Science and Technology VLAIO.

ACKNOWLEDGMENT

Thomas Vandewal and Lars Klijs are kindly acknowledged for their hardware assistance with the ASM Eagle12 PECVD reactor.

ABBREVIATIONS

MOSFET, Metal-Oxide-Semiconductor Field Effect Transistor; BB-TFT, Band-To-Band Tunnel Field-Effect Transistor; CVD, Chemical Vapor Deposition; PEALD, Plasma-Enhanced Atomic Layer Deposition; MX_2, transition metal dichalcogenides; OES, Optical Emission Spectroscopy; RBS, Rutherford Backscattering Spectrometry; SE, Spectroscopic Ellipsometry; XPS, X-ray Photoelectron Spectroscopy; XRD, X-Ray Diffraction; HR-TEM, High-Resolution Transmission Electron Microscopy; PV-TEM, Plan-View Transmission Electron Microscopy; GPC, Growth-Per-Reaction-Cycle; AFM, Atomic Force Microscopy; WW uniformity, Wafer-to-Wafer uniformity; WIW uniformity, Within-Wafer uniformity; ML, monolayer; FWHM, Full-Width-Half-Maximum.

REFERENCES

(1) Hinnemann, B.; Moses, P. G.; Bonde, J.; Jørgensen, K. P.; Nielsen, J. H.; Horch, S.; Chorkendorff, I.; Nørskov, J. K. Biomimetic Hydrogen Evolution: MoS2 Nanoparticles as Catalyst for Hydrogen Evolution. *J. Am. Chem. Soc.* **2005**, *127* (15), 5308–5309.

(2) Chianelli, R. R.; Siadati, M. H.; Rosa, M. P. D. la; Berhault, G.; Wilcoxon, J. P.; Jr, R. B.; Abrams, B. L. Catalytic Properties of Single Layers of Transition Metal Sulfide Catalytic Materials. *Catal. Rev.* **2006**, *48* (1), 1–41.

(3) Jaramillo, T. F.; Jørgensen, K. P.; Bonde, J.; Nielsen, J. H.; Horch, S.; Chorkendorff, I. Identification of Active Edge Sites for Electrochemical H2 Evolution from MoS2 Nanocatalysts. *Science* **2007**, *317* (5834), 100–102.

(4) Wang, Q. H.; Kalantar-Zadeh, K.; Kis, A.; Coleman, J. N.; Strano, M. S. Electronics and Optoelectronics of Two-Dimensional Transition Metal Dichalcogenides. *Nat. Nanotechnol.* **2012**, *7* (11), 699–712.

(5) Lopez-Sanchez, O.; Lembke, D.; Kayci, M.; Radenovic, A.; Kis, A. Ultrasensitive Photodetectors Based on Monolayer MoS2. *Nat. Nanotechnol.* **2013**, *8* (7), 497–501.

(6) Kufer, D.; Konstantatos, G. Highly Sensitive, Encapsulated MoS2 Photodetector with Gate Controllable Gain and Speed. *Nano Lett.* **2015**, *15* (11), 7307–7313.

(7) Radisavljevic, B.; Radenovic, A.; Brivio, J.; Giacometti, V.; Kis, A. Single-Layer MoS2 Transistors. *Nat. Nanotechnol.* **2011**, *6* (3), 147–150.

(8) Radisavljevic, B.; Whitwick, M. B.; Kis, A. Integrated Circuits and Logic Operations Based on Single-Layer MoS2. *ACS Nano* **2011**, *5* (12), 9934–9938.

(9) Ghosh, R. K.; Mahapatra, S. Monolayer Transition Metal Dichalcogenide Channel-Based Tunnel Transistor. *IEEE J. Electron Devices Soc.* **2013**, *1* (10), 175–180.

(10) Roy, T.; Tosun, M.; Cao, X.; Fang, H.; Lien, D.-H.; Zhao, P.; Chen, Y.-Z.; Chueh, Y.-L.; Guo, J.; Javey, A. Dual-Gated MoS2/WSe2 van Der Waals Tunnel Diodes and Transistors. *ACS Nano* **2015**, *9* (2), 2071–2079.

(11) Nourbakhsh, A.; Zubair, A.; Dresselhaus, M. S.; Palacios, T. Transport Properties of a MoS2/WSe2 Heterojunction Transistor and Its Potential for Application. *Nano Lett.* **2016**, *16* (2), 1359–1366.

(12) Sachid, A. B.; Tosun, M.; Desai, S. B.; Hsu, C.-Y.; Lien, D.-H.; Madhvapathy, S. R.; Chen, Y.-Z.; Hettick, M.; Kang, J. S.; Zeng, Y.; He, J.-H.; Chang, E. Y.; Chueh, Y.-L.; Javey, A.; Hu, C. Monolithic 3D CMOS Using Layered Semiconductors. *Adv. Mater.* **2016**, *28* (13), 2547–2554.

(13) Koma, A. Van Der Waals Epitaxy for Highly Lattice-Mismatched Systems. *J. Cryst. Growth* **1999**, *201–202*, 236–241.

(14) Geim, A. K.; Grigorieva, I. V. Van Der Waals Heterostructures. *Nature* **2013**, *499* (7459), 419–425.

(15) Kang, J.; Tongay, S.; Zhou, J.; Li, J.; Wu, J. Band Offsets and Heterostructures of Two-Dimensional Semiconductors. *Appl. Phys. Lett.* **2013**, *102* (1), 12111.

(16) Chhowalla, M.; Shin, H. S.; Eda, G.; Li, L.-J.; Loh, K. P.; Zhang, H. The Chemistry of Two-Dimensional Layered Transition Metal Dichalcogenide Nanosheets. *Nat. Chem.* **2013**, *5* (4), 263–275.

(17) Li, S.-L.; Tsukagoshi, K.; Orgiu, E.; Samorì, P. Charge Transport and Mobility Engineering in Two-Dimensional Transition Metal Chalcogenide Semiconductors. *Chem. Soc. Rev.* **2015**, *45* (1), 118–151.

(18) Chung, J.-W.; Adib, A.; Dai, Z. R.; Adib, K.; Ohuchi, F. S. Raman Scattering and High Resolution Electron Microscopy Studies of Metal-Organic Chemical Vapor Deposition-Tungsten Disulfide Thin Films. *Thin Solid Films* **1998**, *335* (1–2), 106–111.

(19) Yu, Y.; Li, C.; Liu, Y.; Su, L.; Zhang, Y.; Cao, L. Controlled Scalable Synthesis of Uniform, High-Quality Monolayer and Few-Layer MoS2 Films. *Sci. Rep.* **2013**, *3*, 1866.

(20) Kang, K.; Xie, S.; Huang, L.; Han, Y.; Huang, P. Y.; Mak, K. F.; Kim, C.-J.; Muller, D.; Park, J. High-Mobility Three-Atom-Thick Semiconducting Films with Wafer-Scale Homogeneity. *Nature* **2015**, *520* (7549), 656–660.

(21) Park, J.; Lee, W.; Choi, T.; Hwang, S.-H.; Myoung, J. M.; Jung, J.-H.; Kim, S.-H.; Kim, H. Layer-Modulated Synthesis of Uniform Tungsten Disulfide Nanosheet Using Gas-Phase Precursors. *Nanoscale* **2015**, *7* (4), 1308–1313.

(22) Kim, Y.; Song, J.-G.; Park, Y. J.; Ryu, G. H.; Lee, S. J.; Kim, J. S.; Jeon, P. J.; Lee, C. W.; Woo, W. J.; Choi, T.; Jung, H.; Lee, H.-B.-R.; Myoung, J.-M.; Im, S.; Lee, Z.; Ahn, J.-H.; Park, J.; Kim, H. Self-Limiting Layer Synthesis of Transition Metal Dichalcogenides. *Sci. Rep.* **2016**, *6*, 18754.

(23) Mun, J.; Kim, Y.; Kang, I.-S.; Lim, S. K.; Lee, S. J.; Kim, J. W.; Park, H. M.; Kim, T.; Kang, S.-W. Low-Temperature Growth of Layered Molybdenum Disulphide with Controlled Clusters. *Sci. Rep.* **2016**, *6*, 21854.

(24) Chiappe, D.; Asselberghs, I.; Sutar, S.; Iacovo, S.; Afanas'ev, V.; Stesmans, A.; Balaji, Y.; Peters, L.; Heyne, M.; Mannarino, M.; Vandervorst, W.; Sayan, S.; Huyghebaert, C.; Caymax, M.; Heyns, M.; De Gendt, S.; Radu, I.; Thean, A. Controlled Sulfurization Process for the Synthesis of Large Area MoS2 Films and MoS2/WS2 Heterostructures. *Adv. Mater. Interfaces* **2016**, *3* (4), n/a-n/a.

(25) Heyne, M. H.; Chiappe, D.; Meersschaut, J.; Nuytten, T.; Conard, T.; Bender, H.; Huyghebaert, C.; Radu, I. P.; Caymax, M.; Marneffe, J.-F. de; Neyts, E. C.; Gendt, S. D. Multilayer MoS2 Growth by Metal and Metal Oxide Sulfurization. *J. Mater. Chem. C* **2016**, *4* (6), 1295–1304.

(26) George, S. M. Atomic Layer Deposition: An Overview. *Chem. Rev.* **2010**, *110* (1), 111–131.

(27) Puurunen, R. L. Surface Chemistry of Atomic Layer Deposition: A Case Study for the Trimethylaluminum/water Process. *J. Appl. Phys.* **2005**, *97* (12), 121301.

(28) Kessels, E.; Heil, S.; Langereis, E.; Hemmen, H. van; Knoops, H.; Keuning, W.; Sanden, R. van de. Opportunities for Plasma-Assisted Atomic Layer Deposition. *ECS Trans.* **2007**, *3* (15), 183–190.

(29) Scharf, T. W.; Prasad, S. V.; Mayer, T. M.; Goeke, R. S.; Dugger, M. T. Atomic Layer Deposition of Tungsten Disulphide Solid Lubricant Thin Films. *J. Mater. Res.* **2004**, *19* (12), 3443–3446.

(30) Tan, L. K.; Liu, B.; Teng, J. H.; Guo, S.; Low, H. Y.; Loh, K. P. Atomic Layer Deposition of a MoS2 Film. *Nanoscale* **2014**, *6* (18), 10584–10588.

(31) Nandi, D. K.; Sen, U. K.; Choudhury, D.; Mitra, S.; Sarkar, S. K. Atomic Layer Deposited MoS2 as a Carbon and Binder Free Anode in Li-Ion Battery. *Electrochimica Acta* **2014**, *146*, 706–713.

(32) Browning, R.; Plachinda, P.; Padigi, P.; Solanki, R.; Rouvimov, S. Growth of Multiple WS2/SnS Layered Semiconductor Heterojunctions. *Nanoscale* **2016**, *8* (4), 2143–2148.

(33) Delabie, A.; Caymax, M.; Groven, B.; Heyne, M.; Haesevoets, K.; Meersschaut, J.; Nuytten, T.; Bender, H.; Conard, T.; Verdonck, P.; Elshocht, S. V.; Gendt, S. D.; Heyns, M.; Barla, K.; Radu, I.; Thean, A. Low Temperature Deposition of 2D WS2 Layers from WF6 and H2S Precursors: Impact of Reducing Agents. *Chem. Commun.* **2015**, *51* (86), 15692–15695.

(34) Valdivia, A.; Tweet, D. J.; Conley Jr., J. F. Atomic Layer Deposition of Two Dimensional MoS2 on 150 Mm Substrates. *J. Vac. Sci. Technol. Vac. Surf. Films* **2016**, *34* (2), 21515.

(35) Pyeon, J. J.; Kim, S. H.; Jeong, D. S.; Baek, S.-H.; Kang, C.-Y.; Kim, J.-S.; Kim, S. K. Wafer-Scale Growth of MoS2 Thin Films by Atomic Layer Deposition. *Nanoscale* **2016**, *8* (20), 10792–10798.

(36) Jin, Z.; Shin, S.; Kwon, D. H.; Han, S.-J.; Min, Y.-S. Novel Chemical Route for Atomic Layer Deposition of MoS2 Thin Film on SiO2/Si Substrate. *Nanoscale* **2014**, *6* (23), 14453–14458.

(37) Jang, Y.; Yeo, S.; Lee, H.-B.-R.; Kim, H.; Kim, S.-H. Wafer-Scale, Conformal and Direct Growth of MoS2 Thin Films by Atomic Layer Deposition. *Appl. Surf. Sci.* **2016**, *365*, 160–165.

(38) Mackus, A. J. M.; Heil, S. B. S.; Langereis, E.; Knoops, H. C. M.; van de Sanden, M. C. M. Optical Emission Spectroscopy as a Tool for Studying, Optimizing, and Monitoring Plasma-Assisted Atomic Layer Deposition Processes. *J. Vac. Sci. Technol. Vac. Surf. Films* **2009**, *28* (1), 77–87.

(39) Dieke, G. H.; Tomkins, F. S. The Molecular Spectrum of Hydrogen. The Fulcher Bands of TH and ${\mathrm{T}}_{2}$. *Phys. Rev.* **1949**, *76* (2), 283–289.

(40) Xiao, B.; Kado, S.; Kajita, S.; Yamasaki, D. Rovibrational Distribution Determination of H 2 in Low Temperature Plasmas by Fulcher-α Band Spectroscopy. *Plasma Phys. Control. Fusion* **2004**, *46* (4), 653.

(41) loeneninstruments.com. Holey Carbon 300mesh Copper, Product Nr. HC300Cu, Loeneninstruments.com.

(42) Zhang, X.; Qiao, X.-F.; Shi, W.; Wu, J.-B.; Jiang, D.-S.; Tan, P.-H. Phonon and Raman Scattering of Two-Dimensional Transition Metal Dichalcogenides from Monolayer, Multilayer to Bulk Material. *Chem. Soc. Rev.* **2015**, *44* (9), 2757–2785.

(43) Mitioglu, A. A.; Plochocka, P.; Deligeorgis, G.; Anghel, S.; Kulyuk, L.; Maude, D. K. Second-Order Resonant Raman Scattering

in Single-Layer Tungsten Disulfide ${\mathrm{WS}}_{2}$. *Phys. Rev. B* **2014**, *89* (24), 245442.

(44) Tran Khac, B. C.; Jeon, K.-J.; Choi, S. T.; Kim, Y. S.; Del-Rio, F. W.; Chung, K.-H. Laser-Induced Particle Adsorption on Atomically Thin MoS2. *ACS Appl. Mater. Interfaces* **2016**, *8* (5), 2974–2984.

(45) Yu, M. L.; Ahn, K. Y.; Joshi, R. V. Surface Reactions in the Chemical Vapor Deposition of Tungsten Using WF6 and SiH4 on Al, PtSi, and TiN. *J. Appl. Phys.* **1990**, *67* (2), 1055–1061.

(46) Yu, M. L.; Ahn, K. Y.; Joshi, R. V. Surface Chemistry of the WF6-Based Chemical Vapor Deposition of Tungsten. *IBM J. Res. Dev.* **1990**, *34*, 875–883.

(47) Ohshima, H.; Katayama, M.; Onoda, K.; Hattori, T. X-ray Photoelectron Spectroscopic Study of the Chemical Vapor Deposited W/Al Interface. *J. Appl. Phys.* **1993**, *74* (1), 749–751.

(48) Yang, J.; Kim, S.; Choi, W.; Park, S. H.; Jung, Y.; Cho, M.-H.; Kim, H. Improved Growth Behavior of Atomic-Layer-Deposited High-K Dielectrics on Multilayer MoS2 by Oxygen Plasma Pretreatment. *ACS Appl. Mater. Interfaces* **2013**, *5* (11), 4739–4744.

(49) Cheng, L.; Qin, X.; Lucero, A. T.; Azcatl, A.; Huang, J.; Wallace, R. M.; Cho, K.; Kim, J. Atomic Layer Deposition of a High-K Dielectric on MoS2 Using Trimethylaluminum and Ozone. *ACS Appl. Mater. Interfaces* **2014**, *6* (15), 11834–11838.

(50) Zhang, H.; Chiappe, D.; Meersschaut, J.; Conard, T.; Franquet, A.; Nuytten, T.; Mannarino, M.; Radu, I.; Vandervorst, W.; Delabie, A. Nucleation and Growth Mechanisms of Al2O3 Atomic Layerdeposition on Synthetic Polycrystalline MoS2. *J. Chem. Phys.* **2016**, *146* (5), 52810.

(51) Zhao, W.; Ghorannevis, Z.; Amara, K. K.; Pang, J. R.; Toh, M.; Zhang, X.; Kloc, C.; Tan, P. H.; Eda, G. Lattice Dynamics in Mono- and Few-Layer Sheets of WS2 and WSe2. *Nanoscale* **2013**, *5* (20), 9677–9683.

(52) Berkdemir, A.; Gutiérrez, H. R.; Botello-Méndez, A. R.; Perea-López, N.; Elías, A. L.; Chia, C.-I.; Wang, B.; Crespi, V. H.; López-Urías, F.; Charlier, J.-C.; Terrones, H.; Terrones, M. Identification of Individual and Few Layers of WS2 Using Raman Spectroscopy. *Sci. Rep.* **2013**, *3*, 1755.

(53) Alexiev, V.; Prins, R.; Weber, T. DFT Study of MoS2 and Hydrogen Adsorbed on the (100) Face of MoS2. *Phys. Chem. Chem. Phys.* **2001**, *3* (23), 5326–5336.

(54) Sun, M.; Nelson, A. E.; Adjaye, J. Adsorption and Dissociation of H2 and H2S on MoS2 and NiMoS Catalysts. *Catal. Today* **2005**, *105* (1), 36–43.

(55) Keong Koh, E. W.; Chiu, C. H.; Lim, Y. K.; Zhang, Y.-W.; Pan, H. Hydrogen Adsorption on and Diffusion through MoS2 Monolayer: First-Principles Study. *Int. J. Hydrog. Energy* **2012**, *37* (19), 14323–14328.

(56) Green, W. M.; Hess, D. W.; Oldham, W. G. Plasma- and Gas-surface Interactions during the Chemical Vapor Deposition of Tungsten from H2/WF6. *J. Appl. Phys.* **1988**, *64* (9), 4696–4703.

(57) Blume, R.; Niehus, H.; Conrad, H.; Böttcher, A. Oxide-Free Oxygen Incorporation into Ru(0001). *J. Chem. Phys.* **2004**, *120* (8), 3871–3879.

(58) Leick, N.; Agarwal, S.; Mackus, A. J. M.; Potts, S. E.; Kessels, W. M. M. Catalytic Combustion Reactions During Atomic Layer Deposition of Ru Studied Using 18O2 Isotope Labeling. *J. Phys. Chem. C* **2013**, *117* (41), 21320–21330.

(59) Knoops, H. C. M.; Mackus, A. J. M.; Donders, M. E.; Sanden, M. C. M. van de; Notten, P. H. L.; Kessels, W. M. M. Remote Plasma ALD of Platinum and Platinum Oxide Films. *Electrochem. Solid-State Lett.* **2009**, *12* (7), G34–G36.

(60) Erkens, I. J. M.; Mackus, A. J. M.; Knoops, H. C. M.; Smits, P.; Ven, T. H. M. van de; Roozeboom, F.; Kessels, W. M. M. Mass Spectrometry Study of the Temperature Dependence of Pt Film Growth by Atomic Layer Deposition. *ECS J. Solid State Sci. Technol.* **2012**, *1* (6), P255–P262.

(61) Elam, J. W.; Nelson, C. E.; Grubbs, R. K.; George, S. M. Nucleation and Growth during Tungsten Atomic Layer Deposition on SiO2 Surfaces. *Thin Solid Films* **2001**, *386* (1), 41–52.

(62) Grubbs, R. K.; Nelson, C. E.; Steinmetz, N. J.; George, S. M. Nucleation and Growth during the Atomic Layer Deposition of W on Al2O3 and Al2O3 on W. *Thin Solid Films* **2004**, *467* (1–2), 16–27.

(63) Kalanyan, B.; Losego, M. D.; Oldham, C. J.; Parsons, G. N. Low-Temperature Atomic Layer Deposition of Tungsten Using Tungsten Hexafluoride and Highly-Diluted Silane in Argon. *Chem. Vap. Depos.* **2013**, *19* (4–6), 161–166.

(64) Kalanyan, B.; Lemaire, P. C.; Atanasov, S. E.; Ritz, M. J.; Parsons, G. N. Using Hydrogen To Expand the Inherent Substrate Selectivity Window During Tungsten Atomic Layer Deposition. *Chem. Mater.* **2016**, *28* (1), 117–126.

(65) Morosanu, C.-E.; Soltuz, V. Kinetics and Properties of Chemically Vapour-Deposited Tungsten Films on Silicon Substrates. *Thin Solid Films* **1978**, *52* (2), 181–194.

(66) Jiang, J.-W.; Qi, Z.; Park, H. S.; Rabczuk, T. Elastic Bending Modulus of Single-Layer Molybdenum Disulfide (MoS 2): Finite Thickness Effect. *Nanotechnology* **2013**, *24* (43), 435705.

SYNOPSIS TOC (Word Style “SN_Synopsis_TOC”). If you are submitting your paper to a journal that requires a synopsis graphic and/or synopsis paragraph, see the Instructions for Authors on the journal’s homepage for a description of what needs to be provided and for the size requirements of the artwork.

Authors are required to submit a graphic entry for the Table of Contents (TOC) that, in conjunction with the manuscript title, should give the reader a representative idea of one of the following: A key structure, reaction, equation, concept, or theorem, etc., that is discussed in the manuscript. Consult the journal’s Instructions for Authors for TOC graphic specifications.